Majorana corner modes in a second-order Kitaev spin liquid

Vatsal Dwivedi,* Ciarán Hickey, Tim Eschmann, and Simon Trebst
Institute for Theoretical Physics, University of Cologne, 50937 Cologne, Germany

(Received 29 March 2018; published 30 August 2018)

Higher-order topological insulators are distinguished by the existence of topologically protected modes with codimension two or higher. Here, we report the manifestation of a second-order topological insulator in a two dimensional frustrated quantum magnet, which exhibits topological corner modes. Our exactly solvable model is a generalization of the Kitaev honeycomb model to the Shastry-Sutherland lattice that, besides a chiral spin liquid phase, exhibits a gapped spin liquid with Majorana corner modes, which are protected by two mirror symmetries. This second-order Kitaev spin liquid remains stable in the presence of thermal fluctuations and undergoes a finite-temperature phase transition evidenced in large-scale quantum Monte Carlo simulations.

DOI: 10.1103/PhysRevB.98.054432

I. INTRODUCTION

The study of topological band theory for noninteracting electron systems has led to the advent of a plethora of topological insulators (TIs) [1–5]. A central feature of these systems is the existence of gapless boundary modes, which are protected by the topology of the bulk bands, i.e., they cannot be gapped out by any deformation of the Hamiltonian which keeps the bulk gap open and preserves certain symmetries. These systems are termed "topological" because their low energy behavior is governed by a topological action, which is independent of microscopic details of the system such as the underlying lattice structure. However, this is strictly true only for *strong TIs*, which are protected by time reversal and/or charge conjugation symmetries. In recent years, a class of more "fragile" variants of these phases, termed *crystalline TIs*, has been explored. For these systems, the boundary modes are protected only under Hamiltonian deformations that preserve certain lattice symmetries [6], and exist only on boundaries that are themselves invariant under these symmetries. Importantly, for these more fragile systems the crystal structure remains important even for the low-energy physics.

Recently, the family of crystalline TIs has been expanded by what are best called *higher-order topological insulators* [7–9]. In this paradigm, an nth-order TI is a d-dimensional insulator that exhibits topologically protected gapless modes only in $d-n$ spatial dimensions localized at the intersection of n boundary planes, while the boundaries of codimension less than n remain gapped. For instance, a second-order TI (SOTI) in two spatial dimensions is an insulator whose edge state itself is a one-dimensional TI, with zero modes localized only at the corners of the system. Various crystalline symmetries have been invoked for the protection of the zero modes, including order-two lattice symmetries [7,8,10,11] (such as mirror reflection, twofold rotation, or inversion symmetry) or higher-order lattice symmetries such as threefold [12,13], fourfold [9,14,15], and sixfold [16] rotation symmetries. Inspired by this theoretical work, experimental realizations of higher-order TIs have been observed as phononic TI in a cleverly designed mechanical metamaterial [17] and as quantized quadrupolar TIs in electrical [18] and microwave [19] circuits, along with the recent discovery that elemental bismuth is in fact a second-order TI [13].

In this article, we introduce an exactly solvable microscopic spin model of a frustrated quantum magnet, which exhibits an analog of the SOTI in a strongly interacting system. More precisely, our model exhibits spin liquid physics at low temperatures, with a fractionalization of its local degrees of freedom into itinerant Majorana fermions and a static $\mathbb{Z}_2$ gauge field. The band structure of the Majorana fermions reveals a phase diagram with not only a conventional Chern insulator, but also a SOTI with topologically protected corner modes. The former corresponds to the formation of a chiral spin liquid ground state, while the latter is the first instance of a *second-order* spin liquid [20]. Both spin liquids describe states with spontaneously broken time-reversal (TR) symmetry, which are separated from the high-temperature paramagnet by a finite-temperature phase transition. We track this thermal phase transition and the prior spin fractionalization in various thermodynamic observables calculated via sign problem-free quantum Monte Carlo (QMC) simulations of our spin model.

The rest of this article is organized as follows. In Sec. II, we introduce our generalization of the Kitaev honeycomb model to the Shastry-Sutherland lattice and present its exact solution. In Sec. III, we derive the ground state phase diagram and identify various phases. The finite temperature results from QMC are discussed in Sec. IV, and we conclude in Sec. V. Explicit details of the computations have been relegated to the Appendixes.

II. MICROSCOPIC MODEL

We consider a higher-spin realization of the Kitaev honeycomb model [21] to the Shastry-Sutherland lattice [22] illustrated in Fig. 1. This lattice is best known for the orthogonal-dimer model, which has been solved exactly by Shastry and Sutherland [22] and is a remarkably good description for the low-temperature physics of the transition metal oxide

*vdwivedi@thp.uni-koeln.de

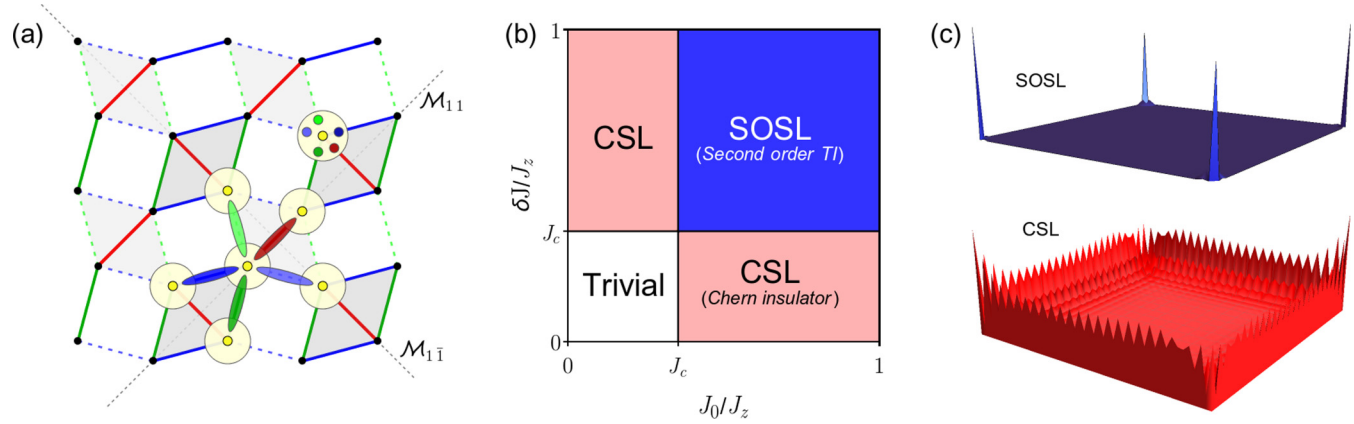

FIG. 1. Higher-order Kitaev model on the Shastry-Sutherland lattice. (a) The Shastry-Sutherland lattice, with the spin x, y, z bonds for the 1D Kitaev chain depicted by solid blue, green, and red lines, respectively, while the orbital x, y bonds are depicted by dashed blue and green lines, respectively. The dark and light gray shading denotes the two kinds of plaquettes with couplings $J_0 + \delta J$ and $J_0 - \delta J$, respectively. The dotted gray lines denote the two mirror axes. (b) The phase diagram as a function of average couplings and staggerings on the rhombi. Here, $J_c = \frac{1}{2\sqrt{2}}$. (c) The zero energy wave functions $|\psi_{ij}|^2$ on a 16×16 lattice for the four corner modes in the SOSL phase and a single zero energy wave function corresponding to the edge mode in the CSL phase.

$SrCu_2(BO_3)_2$ [23]. As a five-coordinated lattice, it shares an *odd* coordination number for every site with the tricoordinated honeycomb lattice, which is a crucial ingredient [24] to construct an exactly solvable Kitaev model. For the honeycomb Kitaev model, the tricoordination of the sites matches perfectly with the decomposition of the original spin-1/2 degrees of freedom into three "bond Majorana fermions," which are recombined into $\mathbb{Z}_2$ gauge fields (assigned to the bonds), and one itinerant Majorana fermion. By analogy, a five-coordinated lattice asks for six Majorana fermions, which in principle span a Hilbert space of eight states. However, keeping in mind that the physical subspace of a Kitaev model needs a projection to precisely half of this Hilbert space, we are looking for constituent degrees of freedom that span a local Hilbert space of only four states. This can be achieved by either considering a $j = 3/2$ spin degree of freedom or, alternatively, two coupled spin-1/2 degrees of freedom, such as spin and orbital degrees of freedom. Using the latter, we first define our microscopic model as

$$\mathcal{H} = \sum_{\langle i,j\rangle} J_\gamma \left(\tau_i^z \tau_j^z\right) \otimes \left(\sigma_i^\gamma \sigma_j^\gamma\right) + \sum_{(i,j)} J'_\delta \tau_i^\delta \tau_j^\delta \otimes \mathbb{1}, \quad (1)$$

where the Pauli matrices σ and τ denote the spin and orbital degrees of freedom and $\langle i, j\rangle$ and (i, j) indicate couplings along the solid/dashed bonds in Fig. 1(a), respectively. Five different bond types that couple spin and orbital components $\gamma \in \{x, y, z\}$ and $\delta \in \{x, y\}$, respectively, are defined as marked in Fig. 1(a). We further allow a staggering of the couplings on the two kinds of rhombi [shaded in dark and light gray in Fig. 1(a)].

In order to solve this model exactly, we first recast it into a Kitaev-like form by defining, for each site, the 4×4 anticommutating matrices,

$$\Gamma^1 = \tau^x \otimes \mathbb{1}, \quad \Gamma^2 = \tau^y \otimes \mathbb{1}, \quad \Gamma^3 = \tau^z \otimes \sigma^x,$$
$$\Gamma^4 = \tau^z \otimes \sigma^y, \quad \Gamma^5 = \tau^z \otimes \sigma^z, \quad (2)$$

so that the Hamiltonian becomes [25,26]

$$\mathcal{H}_{\text{Kitaev}} = -\sum_{\gamma \text{ bonds}} J_\gamma \Gamma_j^\gamma \Gamma_k^\gamma, \quad (3)$$

where $\gamma = 1, \ldots, 5$ labels the $j-k$ bond. Following Kitaev's original solution [21], we represent the Γ matrices in terms of the aforementioned six Majorana operators by setting $\Gamma_j^\gamma = i a_j^\gamma c_j$. The Majoranas associated with the bonds can then be recombined into a $\mathbb{Z}_2$ gauge field $\hat{u}_{jk} \equiv i a_j^\gamma a_k^\gamma$ with eigenvalues $u_{jk} = \pm1$. Like in the honeycomb Kitaev model, this $\mathbb{Z}_2$ gauge field is *static*, since all $\hat{u}_{jk}$ commute with the Hamiltonian. The relevant gauge-invariant quantities are the $\mathbb{Z}_2$ fluxes through the elementary closed loops of the lattice ($0, \pi$ through 4-loops and $\pm\pi/2$ for 3-loops, respectively). The fluxes $\pm\pi/2$ are related by TR, so that any choice of ground state flux configuration breaks the TR symmetry of the Hamiltonian. We next need to identify the precise ground-state configuration of the $\mathbb{Z}_2$ fluxes. Since the lattice at hand does not meet the requirements to apply Lieb's theorem [27] to immediately identify the ground-state configuration, we instead resort to a numerical exact solution of this problem via QMC simulations, described in more detail below. The net result is that each loop of length 4 exhibits a π flux, while for the triangular plaquettes (two of which add up to one 4-loop) the flux is $\pm\pi/2$ [28,29].

The resulting free Majorana Hamiltonian has a particle-hole symmetry, which follows directly from the reality condition for Majorana fermions. Since the TR symmetry is broken spontaneously by the ground state, the system resides in symmetry class D (instead of BDI for the honeycomb Kitaev model). With the systematic classification of TIs [30,31] in mind, symmetry class D allows for a $\mathbb{Z}$ invariant in two spatial dimensions, i.e., the occurrence of Chern insulators, as well as the possibility of a SOTI in the presence of a second-order lattice symmetry [11]. Indeed, the Shastry-Sutherland lattice possesses two mirror symmetries along the diagonals of the rhombi [indicated by the dotted lines in Fig. 1(a)], which are also symmetries of the Majorana Hamiltonian. In particular,

the mirror operators $\mathcal{M}_{11}$ and $\mathcal{M}_{1\bar{1}}$ anticommute with the Hamiltonian as well as with each other (see Appendix A for explicit definitions).

III. GROUND-STATE PHASE DIAGRAM

We next discuss the ground-state phase diagram as a function of the coupling strength J_0 and the staggering δJ, with $J_x = J_y = J_0 + \delta J$ and $J'_x = J'_y = J_0 - \delta J$. Following a Fourier transformation of the four-band itinerant Majorana Hamiltonian, we obtain a bulk band structure, which is gapless along the lines $J_z = \pm 2\sqrt{2} J_0$ [at $\mathbf{k} = (0, 0)$] and $J_z = \pm 2\sqrt{2}\delta J$ [at $\mathbf{k} = (\pi, \pi)$], and gapped otherwise. The four resulting gapped phases are indicated in the phase diagram of Fig. 1(b). The phase diagram is reflection symmetric about the lines $J_0 = \pm \delta J$, since such a reflection is equivalent to a $\mathbb{Z}_2$ gauge transformation.

By a direct computation, we find that the valence band carries a (non-Abelian) Chern number $+1$ in two of these gapped phases, indicated by red in the phase diagram. In terms of the Majorana fermions, these are conventional Chern insulators, while in the language of the original spin model, these phases constitute chiral spin liquids (CSLs) [32]. Discussed previously [25] in the context of the Γ-matrix model (3), these CSLs are higher-spin analogs of the CSL first discovered in a decorated honeycomb model by Yao and Kivelson [33]. While the Chern number vanishes in the two remaining gapped phases, not both of them are trivial. For sufficiently large staggering δJ (i.e., in the upper right corner of the phase diagram), we find a SOTI phase, which, in the language of the original spin model, can be termed a *second-order spin liquid* (SOSL). Computing the spectrum for the real space Hamiltonian on a square with open boundary conditions, we obtain four states near zero energy ($\varepsilon = 0$), separated by a gap from the continuum. The corresponding wave functions are exponentially localized at the corners of the square, as shown in Fig. 1(c). We contrast this with the CSL, where we get a topologically protected chiral mode localized at the edge. We also observe that the SOSL does not exhibit any zero modes on a system with periodic boundary conditions along one or both directions.

The existence of corner modes is a hallmark of SOTIs. These modes can be intuitively understood as a domain wall between two 1D topological phases [10]. To wit, the system exhibits modes localized on mirror symmetric edges [i.e, along a diagonal in Fig. 1(a)], which disperse along the edge and can be described by a $1 + 1$D massless Dirac Hamiltonian. For the (non-mirror-symmetric) edges depicted in Fig. 1(a), these edge modes are gapped out by a mass term. However, since the two edges meeting at a corner are related by a mirror symmetry under which the mass term must be odd, the corner is a mass domain wall in a Dirac Hamiltonian, which explains the presence of the corner mode.

The topologically protected corner modes can also be inferred from the *bulk* bands using the Wannier centers [8]. Explicitly, we compute the hybrid Wannier functions [34], a basis of wave functions localized along x but delocalized along y (or vice versa), and plot their centers $r_x(k_y)$ modulo lattice translations [35], so that zero and 1 correspond to the same Wannier centers. Since the mirror symmetries take $(x, y) \to \pm(y, x)$ and anticommute with Hamiltonian, the

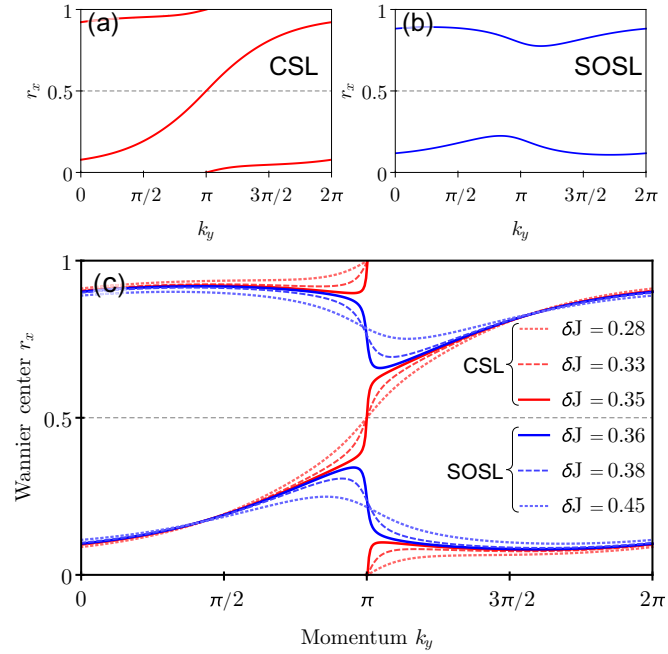

FIG. 2. Wannier bands for (a) the CSL ($\delta J = 0.2$) and (b) the SOSL ($\delta J = 0.5$) phase with $J_0 = 0.8$, $J_z = 1$. Since the Wannier centers zero and 1 are equivalent, the plotted region is topologically a two-torus. The CSL is characterized by a winding of the Wannier bands along the torus, while the SOSL is characterized by gapped Wannier bands along both x and y (not shown). (c) The transition between the CSL and SOSL phases.

Wannier centers along y satisfy $r_y(k) = -r_x(k) \bmod 1$. In Figs. 2(a) and 2(b), we plot the Wannier bands for the CSL and the SOSL phase, which exhibit distinct topologies.

The Wannier bands can then be used to deduce the topological phase. For the CSL (CI), the Wannier band exhibits a nontrivial winding around the torus, but no such winding for the trivial and the SOSL (SOTI) phase. The latter can be distinguished [8] by computing the Berry phase p associated with a Wannier band (see Appendix C). The mirror symmetries restrict this Berry phase to $0, \pi$, which correspond to the trivial and SOSL phase, respectively. For the plot in Fig. 2(b), the Berry phase for both the Wannier bands along x and y is computed to be π, thereby demonstrating a SOSL phase. Finally, as we tune δJ through the CSL-SOSL transition, we see a transition between these two scenarios, where a branch of the winding Wannier band of the CSL detaches and reattaches to a different branch to form the Wannier band structure of the SOSL, as shown in Fig. 2(c).

IV. THERMODYNAMICS

To explore the thermal stability of the SOSL and the finite-temperature transition associated with spontaneous TR symmetry breaking, we have employed large-scale QMC simulations of our spin model, which are sign problem free in the Majorana basis [36]. Our results, summarized in Fig. 3, indicate three relevant temperature scales, each one associated with a peak in the specific heat and a corresponding drop in the entropy per site. At the lowest temperature scale of

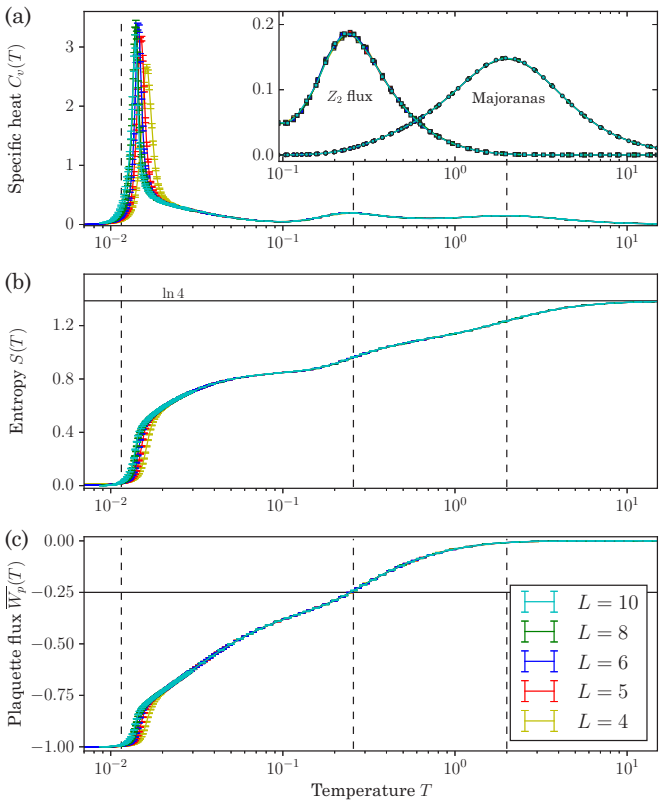

FIG. 3. Thermodynamics of the SOSL. The upper panel shows the specific heat, the middle panel the entropy per spin, and the lower panel the $\mathbb{Z}_2$ flux per plaquette as a function of temperature for $J_0 = 0.9$, $\delta J = 0.4$, and $J_z = 1$. The three characteristic temperature scales for the low-temperature ordering transition (extrapolated to the thermodynamic limit) and the two high-temperature crossovers are indicated by the dashed vertical lines.

$T \approx 0.01 J_z$ the system undergoes a phase transition, at which the $\mathbb{Z}_2$ gauge field orders into its ground-state configuration with a $\pi/2$ flux through all triangular plaquettes and a π flux through all 4-loops; see Fig. 3(c). A finite-size scaling analysis of the specific heat peak indeed reveals a divergence of the peak and a finite transition temperature $T_c = 0.012(1) J_z$ in the thermodynamic limit (see Appendix D). Above this transition, we observe two independent thermodynamic crossovers, indicated by nondiverging peaks around $T_1 \approx 0.25 J_z$ and $T_2 \approx 2 J_z$ in the specific heat; see the inset of Fig. 3(a). The higher crossover can be associated with the release of entropy of the Majorana fermions, whose energy scale is set by the hopping strength J_z, while the lower crossover is associated with a partial release of entropy of the $\mathbb{Z}_2$ gauge field due to the staggering δJ. The appearance of this lower crossover can be best understood by considering the limit $\delta J \to J_0$, in which the system decomposes into decoupled 1D chains (see Appendix B), formed by the dark gray plaquettes connected by the solid bonds in Fig. 1(a). At zero temperature, the individual chains are gapped and exhibit a π flux per tetragonal plaquette [37]. At finite temperature these fluxes, which constitute $1/4$ of the total flux of the 2D system, order at the temperature T_1, while the remaining plaquettes remain disordered. This results in a plateau in the $\mathbb{Z}_2$ flux per plaquette at $-1/4$, which clearly evolves as one approaches the 1D limit (as illustrated in Fig. 6 in Appendix D) and is accompanied by a smooth nondiverging peak in the specific heat (since this 1D physics does not give rise to a true phase transition). When $\delta J \neq J_0$ the remaining 3/4 of the plaquettes order at a much lower temperature scale, giving rise to the actual phase transition at $T \approx 0.01 J_z$.

It is interesting to note that, for the purely 1D tetragonal chain, the $\mathbb{Z}_2$ gauge field freezes into its ground state configuration at a temperature scale of order $O(J)$. This is in marked contrast to the Kitaev model in two and three spatial dimensions where the same phenomenon occurs at $O(10^{-2} J)$ [36,38,39]. The significantly higher temperature scale could have interesting experimental consequences for quasi-1D magnetic materials which realize Kitaev interactions.

V. DISCUSSION

The search for an experimental realization of the second-order Kitaev spin liquid and its clear thermodynamic signatures of fractionalization at comparatively high temperature scales could bring some diversity to the current hunt for Kitaev materials [40]. A natural starting point is to first look for realizations of the Shastry-Sutherland lattice in spin-orbit dominated materials. One step in this direction has been taken by exploring the $4f$ material DyB_4 [41–44], for which the spin-orbit coupling—enhanced by the relatively high atomic number of $Z = 66$ for Dy (compared to $Z = 44/77$ for the Ru-/Ir-based Kitaev materials)—holds promise to give rise to the required bond-directional exchange interactions. Given a suitable candidate material, the experimental detection of the corner modes of a second-order Kitaev spin liquid still poses a number of challenges. The density of states of the emergent Majorana fermions cannot be directly probed by scanning tunneling techniques, in contrast to conventional electronic systems [45]. A more subtle experimental protocol is thus called for, perhaps taking advantage of the emergent quasiparticles' ability to carry heat. Indeed, the challenges mirror many of the problems of detecting emergent Majorana fermions in conventional Kitaev spin liquids, due to their lack of spin or charge quantum numbers.

The study at hand complements previous theoretical work [46] on classifying topological band structures for *gapless* Majorana metals in two- and three-dimensional Kitaev models. Depending on the crystalline symmetries, these systems exhibit semimetals with Dirac [21] or Weyl points [47], nodal lines [48,49], or topological metals with Majorana Fermi surfaces [50]. Together with the present study this underpins the notion that Kitaev spin liquids can realize all known topological band structures in analytically tractable microscopic spin models. As such we expect that one can also construct Kitaev models that realize other higher-order spin liquids, including a SOSL with gapless hinges in three spatial dimensions, which we leave to future studies.

ACKNOWLEDGMENTS

We thank Jan Attig, Piet Brouwer, Max Geier, Victor Chua, Srinidhi Ramamurthy, Taylor Hughes, and D. Khomskii for inspiration and useful discussions, as well as Y. Motome and P. Mishchenko for collaboration on a related numerical

project. We acknowledge partial support from the Deutsche Forschungsgemeinschaft (DFG) within the CRC network TR 183 (Projects No. B01 and No. B03) and SFB 1238 (Project No. C03).

APPENDIX A: LATTICE MODEL

The Shastry-Sutherland lattice can be constructed from a 2D square lattice by adding diagonal bonds in every other square. A more "symmetric" version of this lattice can be constructed by deforming the squares into rhombuses with corner angle θ. The lattice has a four site unit cell, with lattice positions

$$\mathbf{r}_1 = (0,\,0), \quad \mathbf{r}_2 = \tfrac{1}{2}(1,\,-a), \tag{A1}$$

$$\mathbf{r}_3 = \tfrac{1}{2}(b,\,b), \quad \mathbf{r}_4 = \tfrac{1}{2}(a,\,-1), \tag{A2}$$

where $a = \tan\left(\frac{\pi}{4} - \frac{\theta}{2}\right)$ and $b = \sqrt{2}\cos\left(\frac{\theta}{2}\right)\sec\left(\frac{\pi}{4} - \frac{\theta}{2}\right)$. The lattice possesses two mirror symmetries along the diagonals, a twofold and a fourfold rotation symmetry (about the centers of the rhombuses and the squares, respectively), as well as two glide symmetries.

The generalized Kitaev model discussed in the manuscript is solved by decomposing Γ's into six Majoranas, as $\Gamma_j^\gamma = i a_j^\gamma c_j$. This doubles the dimension of the Hilbert space, and the physical Hilbert space is the eigenvalue $+1$ sector of the operator $D_j = i a_j^1 a_j^2 a_j^3 a_j^4 a_j^5 c_j$ for each site j. The ground state flux configuration of the $\mathbb{Z}_2$ gauge field, viz., π flux through the 4-loops and $\pi/2$ through the 3-loops, is realized by setting $u_{jk} = \langle i a_j^\gamma a_k^\gamma \rangle = 1$ whenever j is a lower-numbered site than k. The resulting itinerant Majorana Hamiltonian is

$$\begin{aligned}\mathcal{H} = i \sum_{m,n} [& J_x (c_{m,n,1} c_{m-1,n,2} + c_{m,n,3} c_{m-1,n,4}) \\ & + J_y (c_{m,n,1} c_{m,n-1,4} + c_{m,n,2} c_{m-1,n,3}) \\ & + J'_x (c_{m,n,1} c_{m,n,2} + c_{m,n,3} c_{m,n,4}) \\ & + J'_y (c_{m,n,1} c_{m,n,4} + c_{m,n,2} c_{m,n,3}) \\ & - J_z (c_{m,n,2} c_{m,n,4} + c_{m,n,1} c_{m+1,n-1,3})].\end{aligned} \tag{A3}$$

By a Fourier transform, we get a Bloch Hamiltonian for a four-band model:

$$\mathcal{H} = i \begin{pmatrix} 0 & J'_x + J_x e^{-ik_x} & -J_z e^{-i(k_x - k_y)} & J'_y + J_y e^{ik_y} \\ -J'_x - J_x e^{ik_x} & 0 & J'_y + J_y e^{ik_y} & -J_z \\ J_z e^{i(k_x - k_y)} & -J'_y - J_y e^{-ik_y} & 0 & J'_x + J_x e^{ik_x} \\ -J'_y - J_y e^{-ik_y} & J_z & -J'_x - J_x e^{-ik_x} & 0 \end{pmatrix}, \tag{A4}$$

where $J_x = J_y = J_0 + \delta J$ and $J'_x = J'_y = J_0 - \delta J$. The unitary operators for the mirror symmetries along the 11 and $1\bar{1}$ directions are

$$\mathcal{M}_{11} = \begin{pmatrix} 0 & 0 & 1 & 0 \\ 0 & 1 & 0 & 0 \\ 1 & 0 & 0 & 0 \\ 0 & 0 & 0 & -1 \end{pmatrix}, \quad \mathcal{M}_{1\bar{1}} = \begin{pmatrix} -1 & 0 & 0 & 0 \\ 0 & 0 & 0 & 1 \\ 0 & 0 & 1 & 0 \\ 0 & 1 & 0 & 0 \end{pmatrix}, \tag{A5}$$

which satisfy $\{\mathcal{M}_{11}, \mathcal{M}_{1\bar{1}}\} = 0$.

APPENDIX B: TETRAGONAL 1D CHAINS

Our lattice model on the Shastry-Sutherland lattice reduces to a Kitaev model on a tricoordinated 1D chain for $J'_x = J'_y = 0$ (or equivalently for $\delta J = J_0$). This model is described by the spin-orbit Hamiltonian

$$\mathcal{H} = \sum_{\langle i,j \rangle} J_\gamma \left(\tau_i^z \tau_j^z\right) \otimes \left(\sigma_i^\gamma \sigma_j^\gamma\right), \tag{B1}$$

which can be thought of as a Kitaev model with a background described by an Ising model. The ground state flux sector for this model is identical to the case of the Shastry-Sutherland lattice, viz., π flux through each four plaquette. This model has been previously studied as *tetragonal chains* in Ref. [37].

For $J_x = J_y = 2J_0 > 0$ and $J_z = 1$, we get two gapped phases separated by the gapless point $J_0 = \frac{1}{2\sqrt{2}} \equiv J_c$, with the gap closing at $k = 0$ of the 1D Brillouin zone. These two phases are topologically distinct, and correspond to the bulk polarization being zero or π, which can be calculated as

$$p = \oint \mathrm{Tr}\mathcal{A}, \quad \mathcal{A} = -i \langle u | du \rangle \tag{B2}$$

being the non-Abelian Berry phase of the occupied bands. For a finite chain, depending on the termination, one of these phases exhibits a protected mode at the end. For the embedding of the chain in a finite Shastry-Sutherland lattice, we note that the chain always terminates on a z bond [see Fig. 1(a) of the main text). In this case, for $J_0 > J_c$, the system exhibits a topologically protected mode at the ends of a finite 1D chain, since in the limit of $J_0 \to \infty$ the system reduces to a set of decoupled squares and two leftover sites at the end, which are the end modes. The other phase has no such modes, since for $J_0 \to 0$ the system consists of a set of dimers.

APPENDIX C: WANNIER CENTERS AND BERRY PHASE

A bulk invariant for the SOSL/SOTI phase can be defined in terms of the Wannier band topology of the system. The maximally localized Wannier functions for a one-dimensional system can be defined in terms of a Wilson loop. Given a set of q bands with Bloch wave functions $u_a(\mathbf{k})$, one defines a Wilson loop along k_x as

$$\mathcal{W}_{x,k_0}(k_y) = \mathcal{P} \exp\left\{ \oint_{k_0} \mathcal{A} \right\}, \quad \mathcal{A}_{ab} = -i \langle u_a | du_b \rangle, \tag{C1}$$

where $\mathcal{A}$ denotes the non-Abelian Berry connection, $\mathcal{P}$ denotes the path ordering, and k_0 the base point of the Wilson loop, i.e.,

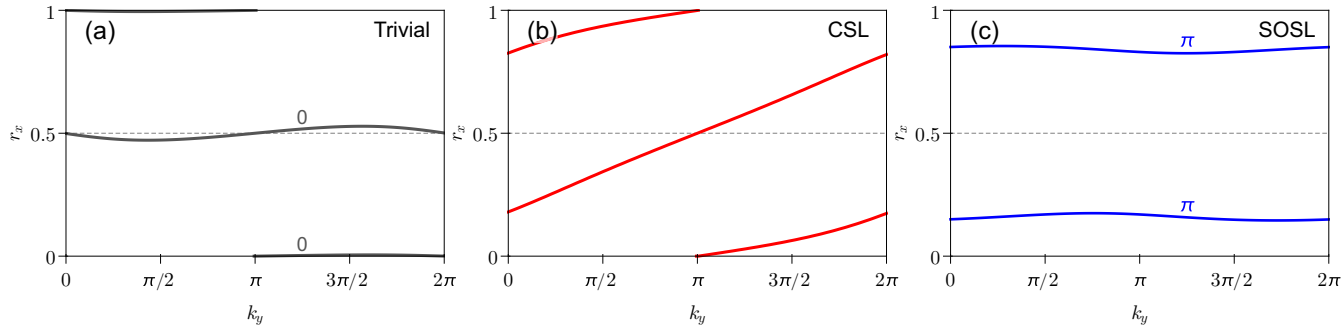

FIG. 4. Wannier bands on various points on the line defined by $\delta J = 0.9J_0$: (a) trivial SL ($J_0 = 0.30$), (b) CSL ($J_0 = 0.37$), and (c) SOSL ($J_0 = 0.60$). Both the trivial spin liquid and the SOSL exhibit gapped Wannier bands which have a winding number zero in r_x, but they can be distinguished by the Berry phase (nested Wilson loop) of the individual Wannier bands, which is zero for the trivial case and π for the SOSL case (as labeled in the figure).

the loop integral is performed from $k_x = k_0$ to $k_x = k_0 + 2\pi$. The Wilson loop is a $q \times q$ unitary matrix, so that its eigenvalues lie on the unit circle, i.e.,

$$\mathcal{W}_{x,k_x}(k_y)\Phi(k_x, k_y) = e^{2\pi i r_x(k_y)}\Phi(k_x k_y),$$

which defines the Wannier center $r_x(k_y) \in [0, 1)$ parametrized by k_y, which is referred to as the *Wannier band*. This definition is independent of the choice of a base point k_x, since the Wilson loops with different base points are related by unitary transformations. An efficient recipe for a numerical computation of the Wannier bands is discussed in Refs. [8,34].

In Fig. 4, we plot the Wannier bands for the three phases of the generalized Kitaev model on the Shastry-Sutherland lattice. Note that the Wannier band has a nonzero winding number along r_x for the CSL phase, while the winding number is zero for the other two phases. The SOSL phase can be distinguished from the trivial SL phase by the Berry phase associated with one of the Wannier bands (also termed a *nested Wilson loop*), well defined only for gapped Wannier bands. Explicitly, let $\Phi(k_y)$ be an eigenvector of $\mathcal{W}_x$ associated with a Wannier band, and define $v(\mathbf{k}) = \sum_a \Phi_a(\mathbf{k})u_a(\mathbf{k})$, with $a = 1, \ldots, q$. The nested Wilson loop is then defined as

$$\widetilde{\mathcal{W}}_y(k_x) \equiv \mathcal{P}\exp\left\{\oint \widetilde{\mathcal{A}}\right\}, \tag{C2}$$

where $\widetilde{\mathcal{A}} = -i\langle v|dv\rangle$ is the nested Berry connection and the integral is now performed over a loop along k_y (for the original Wilson loop along k_x). Defining its eigenvalues as $e^{2\pi i \widetilde{r}_y(k_x)}$, the SOSL invariant is simply

$$p = \oint dk_x \widetilde{r}_y(k_x), \tag{C3}$$

computed over a loop along k_x. A nonzero value of p signifies that the Wannier centers are not aligned with the lattice positions. In the presence of certain lattice symmetries, p is restricted to $0, \pi$, which indicate the trivial and second order phases, respectively.

APPENDIX D: NUMERICAL ANALYSIS

For our numerical analysis of thermodynamic observables, we have employed large-scale quantum Monte Carlo simulations. In this appendix, we describe the numerical setup as well as additional results.

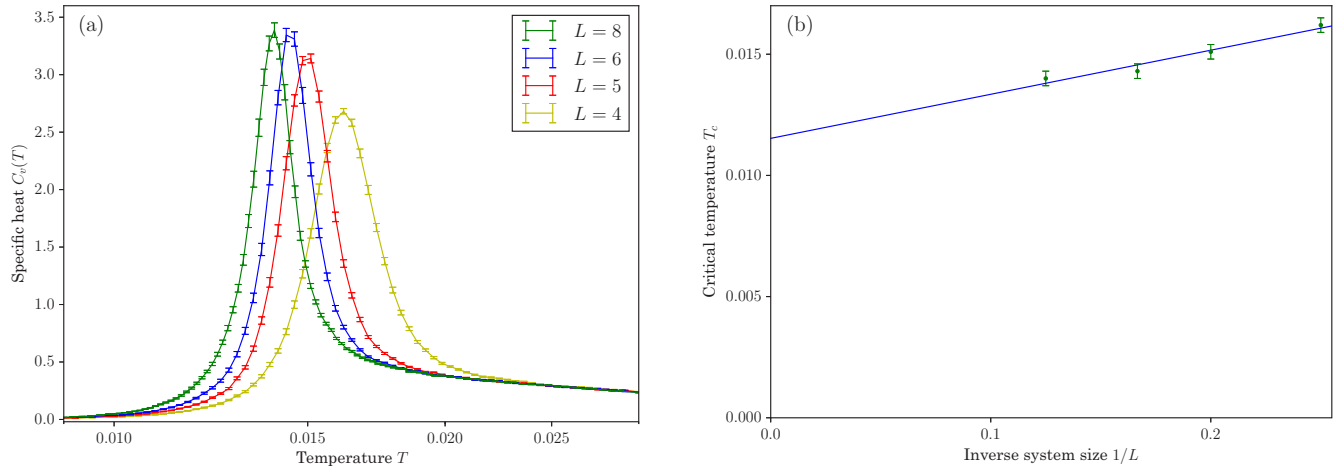

FIG. 5. Finite-size scaling analysis. (a) Gauge field contribution to the specific heat around the low-temperature peak for different system sizes L. (b) Scaling plot of the peak position versus the inverse system size $1/L$. The solid line indicates a linear fit.

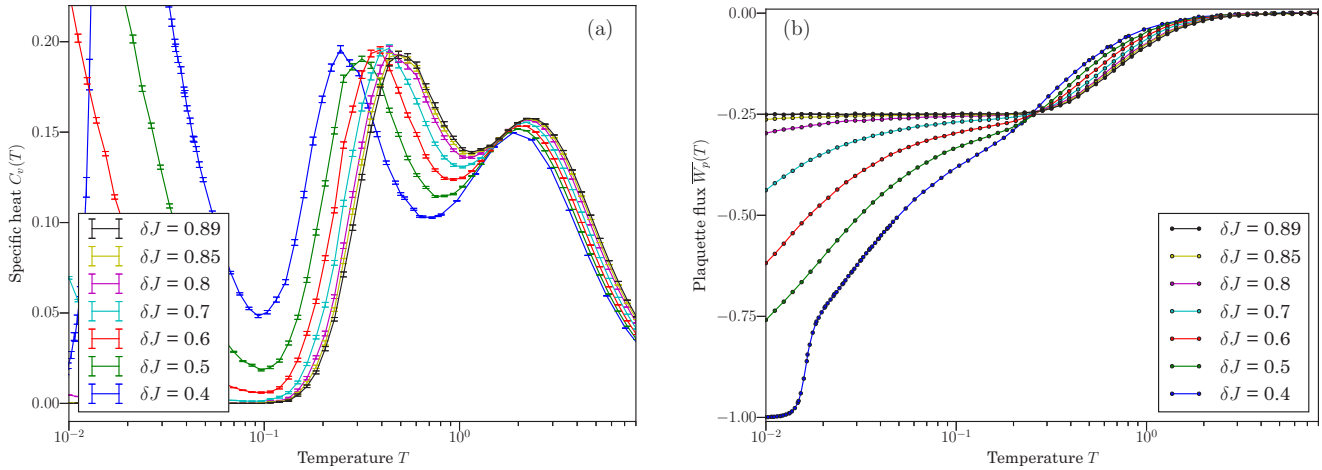

FIG. 6. Approaching the 1D limit. (a) Specific heat and (b) plaquette flux as one approaches the 1D limit $\delta J \to J$ for $J_0 = 0.9$.

1. Monte Carlo approach

The Monte Carlo simulations are sign-problem free in the Majorana basis. In this approach, which has been spearheaded in Ref. [36], one samples configurations $\{u_{jk}\}$ of the $\mathbb{Z}_2$ gauge field with the statistical weight for each configuration calculated via an exact diagonalization of the Majorana fermions. Specifically, the Hamiltonian in a fixed gauge field configuration is diagonalized to a canonical form [21]

$$\mathcal{H} = \sum_{\lambda=1}^{N/2} \epsilon_\lambda \left(a_\lambda^\dagger a_\lambda - \frac{1}{2} \right), \tag{D1}$$

where N denotes the number of spins in the system, while $a_\lambda^\dagger, a_\lambda$ are the creation and annihilation operators of spinless fermions, each one composed of two itinerant Majorana modes. The partition function of the full system can be written as

$$\mathcal{Z} = \mathrm{tr}_{\{u_{jk}\}} \mathrm{tr}_{\{c_i\}} e^{-\beta \mathcal{H}} = \mathrm{tr}_{\{u_{jk}\}} e^{-\beta F(\{u_{jk}\})}, \tag{D2}$$

where $F(\{u_{jk}\})$ denotes the free energy of the itinerant Majorana fermions in a given $\mathbb{Z}_2$ gauge field configuration. The free energy F and all other thermodynamic observables are derived from the partition function of the Majorana system in a fixed $\{u_{jk}\}$ which is obtained via the explicit summation over all fermionic Fock states

$$\mathcal{Z}_{\{c_i\}} = \prod_{\lambda=1}^{N/2} 2 \cosh\left(\frac{\beta \epsilon_\lambda}{2} \right). \tag{D3}$$

The energy of the Majorana system is then given by

$$E_F(\{u_{jk}\}) = -\sum_\lambda \frac{\epsilon_\lambda}{2} \tanh\left(\frac{\beta \epsilon_\lambda}{2} \right). \tag{D4}$$

In order to separate the specific heat contribution of the itinerant Majorana fermions from the fluctuations in the $\mathbb{Z}_2$ gauge field, we calculate [51]

$$\begin{aligned} C_{v,F}(T) &= \frac{1}{T^2} \left(\langle E^2(\{u_{jk}\}) \rangle_F - \langle E(\{u_{jk}\}) \rangle_F^2 \right) \\ &= \frac{1}{T^2} \sum_\lambda \frac{\epsilon_\lambda^2}{4} \left(1 - \tanh^2 \left(\frac{\beta \epsilon_\lambda}{2} \right) \right) \\ &= -\frac{1}{T^2} \frac{\partial E_f(\{u_{jk}\})}{\partial \beta}, \end{aligned} \tag{D5}$$

which gives a total specific heat of

$$C_v(T) = \frac{1}{T^2} \left(\underbrace{\langle E_F^2(\{u_{jk}\}) \rangle_{MC} - \langle E_F(\{u_{jk}\}) \rangle_{MC}^2}_{\text{gauge field contribution}} - \underbrace{\left\langle \frac{\partial E_f(\{u_{jk}\})}{\partial \beta} \right\rangle_{MC}}_{\text{it. Majorana contribution}} \right). \tag{D6}$$

We note that in deriving the Majorana partition function, we have not distinguished between physical and unphysical fermionic Fock states. It is well known that a given $\mathbb{Z}_2$ gauge field configuration on a system with certain boundary conditions allows for either even or odd fermionic parity states [52], with only one of the two constituting the physical states. The unphysical states, which correspond to states of the expanded Hilbert space, contribute deviations of order $1/N$ [53] to observables and can be neglected in the thermodynamic limit.

2. Results

All the simulations were performed on systems with periodic boundary conditions. To avoid the slowing down and freezing of the Monte Carlo sampling at low temperatures, we employed parallel tempering with 24–64 replicas in each simulation. For all the systems, 20 000 measurement sweeps were performed (after 10 000 thermalization sweeps), with every sweep being followed by an attempted replica exchange. The estimate for the critical temperature in the thermodynamic limit was obtained from linear extrapolation of the position of

the low-temperature peak of the specific heat versus the inverse system size $1/L$, as illustrated in Fig. 5(b).

The approach to the 1D limit of the model for $\delta J \to J$ is illustrated in Fig. 6, which shows the specific heat and plaquette flux for $J_0 = 0.9$ and different values of δJ. While the low-temperature crossover of the specific heat peak wanders towards $T_1 \approx 0.55 J_z$, a plateau at $-1/4$ forms in the plaquette flux (Fig. 3).

[1] C. L. Kane and E. J. Mele, $\mathbb{Z}_2$ Topological Order and the Quantum Spin Hall Effect, Phys. Rev. Lett. **95**, 146802 (2005).

[2] L. Fu, C. L. Kane, and E. J. Mele, Topological Insulators in Three Dimensions, Phys. Rev. Lett. **98**, 106803 (2007).

[3] M. Z. Hasan and C. L. Kane, Topological insulators, Rev. Mod. Phys. **82**, 3045 (2010).

[4] X.-L. Qi and S.-C. Zhang, Topological insulators and superconductors, Rev. Mod. Phys. **83**, 1057 (2011).

[5] B. A. Bernevig, *Topological Insulators and Topological Superconductors* (Princeton University Press, Princeton, NJ, 2013).

[6] L. Fu, Topological Crystalline Insulators, Phys. Rev. Lett. **106**, 106802 (2011).

[7] W. A. Benalcazar, B. A. Bernevig, and T. L. Hughes, Quantized electric multipole insulators, Science **357**, 61 (2017).

[8] W. A. Benalcazar, B. A. Bernevig, and T. L. Hughes, Electric multipole moments, topological multipole moment pumping, and chiral hinge states in crystalline insulators, Phys. Rev. B **96**, 245115 (2017).

[9] F. Schindler, A. M. Cook, M. G. Vergniory, Z. Wang, S. S. Parkin, B. A. Bernevig, and T. Neupert, Higher-order topological insulators, Sci. Adv. **4**, eaat0346 (2018).

[10] J. Langbehn, Y. Peng, L. Trifunovic, F. von Oppen, and P. W. Brouwer, Reflection-Symmetric Second-Order Topological Insulators and Superconductors, Phys. Rev. Lett. **119**, 246401 (2017).

[11] M. Geier, L. Trifunovic, M. Hoskam, and P. W. Brouwer, Second-order topological insulators and superconductors with an order-two crystalline symmetry, Phys. Rev. B **97**, 205135 (2018).

[12] M. Ezawa, Higher-Order Topological Insulators and Semimetals on the Breathing Kagome and Pyrochlore Lattices, Phys. Rev. Lett. **120**, 026801 (2018).

[13] F. Schindler, Z. Wang, M. G. Vergniory, A. M. Cook, A. Murani, S. Sengupta, A. Y. Kasumov, R. Deblock, S. Jeon, I. Drozdov, H. Bouchiat, S. Guéron, A. Yazdani, B. A. Bernevig, and T. Neupert, Higher-order topology in bismuth, Nat. Phys. (2018), doi:10.1038/s41567-018-0224-7.

[14] Z. Song, Z. Fang, and C. Fang, $(d-2)$-Dimensional Edge States of Rotation Symmetry Protected Topological States, Phys. Rev. Lett. **119**, 246402 (2017).

[15] M. Ezawa, Magnetic second-order topological insulators and semimetals, Phys. Rev. B **97**, 155305 (2018).

[16] M. Ezawa, Strong and weak second-order topological insulators with hexagonal symmetry and $\mathbb{Z}_3$ index, Phys. Rev. B **97**, 241402(R) (2018).

[17] M. Serra-Garcia, V. Peri, R. Süsstrunk, O. R. Bilal, T. Larsen, L. G. Villanueva, and S. D. Huber, Observation of a phononic quadrupole topological insulator, Nature (London) **555**, 342 (2018).

[18] S. Imhof, C. Berger, F. Bayer, J. Brehm, L. Molenkamp, T. Kiessling, F. Schindler, C. H. Lee, M. Greiter, T. Neupert, and R. Thomale, Topolectrical circuit realization of topological corner modes, arXiv:1708.03647.

[19] C. W. Peterson, W. A. Benalcazar, T. L. Hughes, and G. Bahl, A quantized microwave quadrupole insulator with topologically protected corner states, Nature (London) **555**, 346 (2018).

[20] The second-order spin liquid is an example of a "symmetry-enriched topological" (SET) phase, a phase with intrinsic topological order enriched by the presence of additional symmetries, in this case additional lattice symmetries.

[21] A. Kitaev, Anyons in an exactly solved model and beyond, Ann. Phys. (NY) **321**, 2 (2006), January Special Issue.

[22] B. S. Shastry and B. Sutherland, Exact ground state of a quantum mechanical antiferromagnet, Physica B+C **108**, 1069 (1981).

[23] H. Kageyama, K. Yoshimura, R. Stern, N. V. Mushnikov, K. Onizuka, M. Kato, K. Kosuge, C. P. Slichter, T. Goto, and Y. Ueda, Exact Dimer Ground State and Quantized Magnetization Plateaus in the Two-Dimensional Spin System $SrCu_2(BO_3)_2$, Phys. Rev. Lett. **82**, 3168 (1999).

[24] Analytically tractable generalizations of the Kitaev model to lattices with an even coordination number have been put forward in Refs. [54–56].

[25] C. Wu, D. Arovas, and H.-H. Hung, Γ-matrix generalization of the Kitaev model, Phys. Rev. B **79**, 134427 (2009).

[26] Z. Nussinov and G. Ortiz, Bond algebras and exact solvability of Hamiltonians: Spin $S = \frac{1}{2}$ multilayer systems, Phys. Rev. B **79**, 214440 (2009).

[27] E. H. Lieb, Flux Phase of the Half-Filled Band, Phys. Rev. Lett. **73**, 2158 (1994).

[28] This flux assignment is what Lieb's theorem would dictate, were it applicable.

[29] This ground state of the $\mathbb{Z}_2$ fluxes is separated from all other flux configurations by a finite vision gap for all coupling parameters.

[30] A. P. Schnyder, S. Ryu, A. Furusaki, and A. W. W. Ludwig, Classification of topological insulators and superconductors in three spatial dimensions, Phys. Rev. B **78**, 195125 (2008).

[31] A. Kitaev, Periodic table for topological insulators and superconductors, AIP Conf. Proc. No. 1134 (AIP, Melville, NY, 2009), p. 22.

[32] We restrict the term *chiral spin liquid* to systems which possess a chiral edge mode, and call systems with broken TR symmetry but no edge mode a *trivial chiral spin liquid*.

[33] H. Yao and S. A. Kivelson, Exact Chiral Spin Liquid with Non-Abelian Anyons, Phys. Rev. Lett. **99**, 247203 (2007).

[34] N. Marzari, A. A. Mostofi, J. R. Yates, I. Souza, and D. Vanderbilt, Maximally localized Wannier functions: Theory and applications, Rev. Mod. Phys. **84**, 1419 (2012).

[35] For details, see Sec. II A of Ref. [57] or Sec. IV of Ref. [8].

[36] J. Nasu, M. Udagawa, and Y. Motome, Vaporization of Kitaev Spin Liquids, Phys. Rev. Lett. **113**, 197205 (2014).

[37] A. Saket, S. R. Hassan, and R. Shankar, Manipulating unpaired Majorana fermions in a quantum spin chain, Phys. Rev. B **82**, 174409 (2010).

[38] J. Nasu and Y. Motome, Thermodynamics of Chiral Spin Liquids with Abelian and Non-Abelian Anyons, Phys. Rev. Lett. **115**, 087203 (2015).

[39] P. A. Mishchenko, Y. Kato, and Y. Motome, Finite-temperature phase transition to a Kitaev spin liquid phase on a hyperoctagon lattice: A large-scale quantum Monte Carlo study, Phys. Rev. B **96**, 125124 (2017).

[40] S. Trebst, Kitaev materials, arXiv:1701.07056.

[41] R. Watanuki, G. Sato, K. Suzuki, M. Ishihara, T. Yanagisawa, Y. Nemoto, and T. Goto, Geometrical quadrupolar frustration in DyB_4, J. Phys. Soc. Jpn. **74**, 2169 (2005).

[42] D. Okuyama, T. Matsumura, H. Nakao, and Y. Murakami, Quadrupolar frustration in Shastry Sutherland lattice of DyB_4 studied by resonant x-ray scattering, J. Phys. Soc. Jpn. **74**, 2434 (2005).

[43] S. Ji, C. Song, J. Koo, J. Park, Y. J. Park, K.-B. Lee, S. Lee, J.-G. Park, J. Y. Kim, B. K. Cho, K.-P. Hong, C.-H. Lee, and F. Iga, Resonant X-Ray Scattering Study of Quadrupole-Strain Coupling in DyB_4, Phys. Rev. Lett. **99**, 076401 (2007).

[44] H. Sim, S. Lee, K.-P. Hong, J. Jeong, J. R. Zhang, T. Kamiyama, D. T. Adroja, C. A. Murray, S. P. Thompson, F. Iga, S. Ji, D. Khomskii, and J.-G. Park, Spontaneous structural distortion of the metallic Shastry-Sutherland system DyB_4 by quadrupole-spin-lattice coupling, Phys. Rev. B **94**, 195128 (2016).

[45] S. Nadj-Perge, I. K. Drozdov, J. Li, H. Chen, S. Jeon, J. Seo, A. H. MacDonald, B. A. Bernevig, and A. Yazdani, Observation of Majorana fermions in ferromagnetic atomic chains on a superconductor, Science **346**, 602 (2014).

[46] K. O'Brien, M. Hermanns, and S. Trebst, Classification of gapless $\mathbb{Z}_2$ spin liquids in three-dimensional Kitaev models, Phys. Rev. B **93**, 085101 (2016).

[47] M. Hermanns, K. O'Brien, and S. Trebst, Weyl Spin Liquids, Phys. Rev. Lett. **114**, 157202 (2015).

[48] S. Mandal and N. Surendran, Exactly solvable Kitaev model in three dimensions, Phys. Rev. B **79**, 024426 (2009).

[49] M. G. Yamada, V. Dwivedi, and M. Hermanns, Crystalline Kitaev spin liquids, Phys. Rev. B **96**, 155107 (2017).

[50] M. Hermanns and S. Trebst, Quantum spin liquid with a Majorana Fermi surface on the three-dimensional hyperoctagon lattice, Phys. Rev. B **89**, 235102 (2014).

[51] Y. Shimomura, S. Miyahara, and N. Furukawa, Frustration-induced dodecamer ordering in the double-exchange spin ice model on the kagome lattice, J. Phys. Soc. Jpn. **74**, 661 (2005).

[52] F. L. Pedrocchi, S. Chesi, and D. Loss, Physical solutions of the Kitaev honeycomb model, Phys. Rev. B **84**, 165414 (2011).

[53] F. Zschocke and M. Vojta, Physical states and finite-size effects in Kitaev's honeycomb model: Bond disorder, spin excitations, and NMR line shape, Phys. Rev. B **92**, 014403 (2015).

[54] H. Yao, S.-C. Zhang, and S. A. Kivelson, Algebraic Spin Liquid in an Exactly Solvable Spin Model, Phys. Rev. Lett. **102**, 217202 (2009).

[55] S. Ryu, Three-dimensional topological phase on the diamond lattice, Phys. Rev. B **79**, 075124 (2009).

[56] R. Nakai, S. Ryu, and A. Furusaki, Time-reversal symmetric Kitaev model and topological superconductor in two dimensions, Phys. Rev. B **85**, 155119 (2012).

[57] M. Taherinejad, K. F. Garrity, and D. Vanderbilt, Wannier center sheets in topological insulators, Phys. Rev. B **89**, 115102 (2014).